

# Scalable Synthesis of Supported Catalysts using Fluidized Bed Atomic Layer Deposition

Zheng Lu,<sup>1</sup> Angel Yanguas-Gil,<sup>1</sup> Donghyeon Kang,<sup>1</sup> Pragathi Darapaneni,<sup>1</sup> Anil U. Mane,<sup>1</sup> Christopher L. Marshall,<sup>2</sup> and Jeffrey W. Elam<sup>1,a)</sup>

<sup>1</sup>Applied Materials Division, Argonne National Laboratory, Lemont, Illinois 60439, United States

<sup>2</sup>Chemical Sciences and Engineering Division, Argonne National Laboratory, Lemont, Illinois 60439, United States

a) Electronic mail: [jelam@anl.gov](mailto:jelam@anl.gov)

## ABSTRACT

Overcoating layers deposited on the surface of heterogeneous catalysts using atomic layer deposition (ALD) have been shown to increase catalyst activity, lifetime, and selectivity. In this study, we performed Al<sub>2</sub>O<sub>3</sub> ALD and Pd ALD in a commercial fluidized bed reactor on high surface area mesoporous powder supports to create overcoated catalysts with high precursor utilization. We investigated the reaction mechanism for both the Al<sub>2</sub>O<sub>3</sub> ALD and the Pd ALD using *in-situ* mass spectrometry and developed a mathematical model to understand the precursor saturation behaviors. We characterized the catalyst samples using a variety of techniques to measure the surface area, porosity, composition, and surface chemistry of the overcoated catalysts. Finally, we used propane dehydrogenation as a probe reaction to evaluate the performance of the catalysts prepared by fluidized bed ALD.

## I. INTRODUCTION

Atomic layer deposition (ALD) is a gas-phase technique to deposit conformal thin films or nanoparticles with atomic level precision using sequential, self-limiting surface reactions. Due to its advantages, such as uniform deposition on high aspect ratio substrates,

atomic level thickness control, a wide materials palette, and scalability for manufacturing, ALD has emerged as a powerful synthesis tool in numerous applications including microelectronics, lithium ion batteries, fuel cells, and heterogeneous catalysts.<sup>1-3</sup> The use of ALD for synthesizing highly efficient catalysts has been demonstrated, and examples include bimetallic and core-shell structures, single-atom catalysts, and protective overcoating layers.<sup>4-13</sup> Metallic nanoparticles with high dispersion serve as the active sites in many heterogeneous catalysts, and these nanoparticles are typically prepared on high surface area powder supports permeated with meso- and micropores. Most ALD coating systems are designed for coating planar, low surface area substrates such as silicon wafers.<sup>14</sup> Considering the slow diffusion of ALD precursor vapors and products into and away from porous structures, depositing ALD coatings on porous supports to prepare heterogeneous catalysts typically requires modification of both the ALD process and reactor.

Despite these challenges, conventional ALD systems can be used to coat powders, especially in smaller quantities. For instance, the powder can be uniformly spread into a thin layer in a sample tray, and a wire mesh placed on top of the tray to contain the powder while providing diffusional transport of the ALD precursors and product gases in and out.<sup>15-17</sup> To ensure adequate penetration of the precursors into the nanopores of the powder substrate, and to account for the high surface area of the powder, longer dose and purge times are used compared to coating planar substrates. For substrates with very high aspect ratio pores but a low surface area, such as anodic aluminum oxide, isolation of the ALD chamber from the downstream vacuum pump helps to maximize the precursor usage by giving long soak times.<sup>18</sup> As the depth of the powder bed increases inside the sample tray,

infiltration of the powder bed by the ALD precursors is hindered and can result in thinner coatings deeper into the bed. To address this problem, techniques have been developed to overcome diffusion limitations and homogeneity issues in coating powder samples. One approach is to use a rotary drum ALD reactor, which allows long precursor exposure times while keeping the powder agitated.<sup>19, 20</sup> For a given precursor partial pressure, the amount of precursor for each dose is limited by the reactor volume, thus, multiple repeats of dose and soak are often required when coating higher surface area powders using a rotary drum ALD reactor. Another approach is based on the concept of spatial ALD where the precursors and inert carrier gas are supplied continuously at different physical locations, and the ALD coating is achieved by moving the powder through different spatial domains of chemical composition. In this method, the precursor dose and purge can take place simultaneously at different locations leading to higher throughput.<sup>21</sup> Van Ommen et al. proposed a configuration using a winding tube as the reactor, and the powder was exposed to alternating precursor and purge regions as it moved through the tube.<sup>22</sup>

Alternatively, fluidized bed ALD reactors have been developed to homogeneously coat powders.<sup>23, 24</sup> In fluidized bed ALD, a vertically directed flow of carrier gas is applied to the powder to create an upward drag force that equals the gravitational force due to the mass of the powder. This induces fluidization and improves the rate of physical mixing between the ALD precursors and powder. Moreover, fluidization improves heat exchange to eliminate temperature gradients inside the ALD reactor and to dissipate exothermic heat released during the ALD surface reactions.<sup>23-25</sup> *In-situ* mass spectrometry has been used previously in fluidized bed ALD systems to monitor the concentrations of the ALD

precursors and gaseous reaction products.<sup>24</sup> A variant of fluidized bed ALD, termed semi-continuous ALD, has been demonstrated at the scale of tons per day.<sup>26</sup>

In this study, we performed Al<sub>2</sub>O<sub>3</sub> ALD in a fluidized bed on Pt catalysts supported on mesoporous silica powders to create overcoated catalysts. We also performed Pd ALD followed by Al<sub>2</sub>O<sub>3</sub> ALD on mesoporous alumina powders to create overcoated Pd catalysts in a fluidized bed. We used *in-situ* mass spectrometry to monitor the Al<sub>2</sub>O<sub>3</sub> ALD and Pd ALD surface reactions in real time to study the saturation behavior and mechanism of the ALD reactions. A model was developed to understand the saturation behavior based on different experimental parameters. We examined the surface area and pore size of the catalysts using BET nitrogen adsorption measurements. Thermogravimetric analysis (TGA) was used to monitor the moisture content of the powder samples. The chemical composition of the catalyst surfaces was studied using X-ray photoelectron spectroscopy (XPS) measurements. We used diffuse reflection infrared Fourier transform spectroscopy (DRIFTS) measurements following CO chemisorption and H<sub>2</sub> chemisorption measurements to characterize the metal nanoparticle surfaces. Finally, we used propane dehydrogenation as a probe reaction to evaluate the performance of the catalysts prepared by fluidized bed ALD. We believe this is the first study combining fluidized bed ALD catalyst synthesis, characterization, and testing with *in-situ* measurements to investigate the surface chemistry and analytical modeling to predict the evolution with time of surface coverage, precursor pressure, and product formation.

## **II. EXPERIMENTAL**

### **A. Catalyst Synthesis**

#### **1. Synthesis of Pt/SiO<sub>2</sub> catalyst**

Pt/SiO<sub>2</sub> catalysts were prepared using spherical silica gel (Silicycle S10040M, surface area: 94 m<sup>2</sup>/g, average pore volume: 0.72 cc/g, average pore size: 27.6 nm) as the catalyst support. The Pt/SiO<sub>2</sub> catalysts were prepared by incipient wetness impregnation. Platinum with target weight loading of 0.1% was impregnated using H<sub>2</sub>PtCl<sub>6</sub> (Sigma-Aldrich) on 5.5 g of the support. The material was then dried in air at 110 °C for 12 h followed by calcination in air at 500 °C for 2 h. By repeating the same steps, a second batch of catalyst was made to produce a total of 11 g of Pt/SiO<sub>2</sub> catalyst.

## 2. *Synthesis of 5cAl<sub>2</sub>O<sub>3</sub>/Pt/SiO<sub>2</sub> catalyst*

The Pt/SiO<sub>2</sub> catalysts were overcoated using Al<sub>2</sub>O<sub>3</sub> ALD in a fluidized bed ALD reactor (ForgeNano Prometheus). The reactor is cylindrical in shape with an internal diameter of 4.75 cm and total volume of 150 ml. 10 g of Pt/SiO<sub>2</sub> catalyst was loaded into the reactor. The volume of the catalyst powder was ~15 ml and occupied ~10% of the reactor volume. A distribution plate with 2 μm pore diameter at the bottom and a metal filter at the top of the tubular reactor were used to contain the powder. Ultrahigh purity nitrogen (Airgas, 99.999%) was used as carrier gas and was directed vertically through the tubular reactor to fluidize the powder. The fluidization behavior of the powder was visually observed through a glass window installed temporarily on the top of the reactor. The flow rate was set to 50 sccm to fluidize 10 g of the catalyst powder. The Al<sub>2</sub>O<sub>3</sub> ALD was performed using alternating exposure to 28 min of trimethylaluminum (TMA, Sigma-Aldrich, 97%) and 17 min of deionized water separated by 36 min purge times at 200 °C. Prior to the ALD, the catalyst was fluidized for 30 min at 200 °C. The TMA and H<sub>2</sub>O exposure times were determined to saturate the 10 g of catalyst powder using *in-situ* mass spectrometry measurements as described later. The TMA and H<sub>2</sub>O were supplied through

separate manifolds each having a fluidization mass flow controller and a Baratron capacitance manometer pressure gauge. During the TMA exposures, a pneumatic valve was opened to allow the TMA to flow into the manifold where it was transported to the reactor by the carrier gas flow. A similar arrangement was used to supply the H<sub>2</sub>O. The TMA and H<sub>2</sub>O containers were heated to 40 °C to provide sufficient vapor pressures. According to the Antoine equation, the TMA and H<sub>2</sub>O vapor pressures at 40 °C are ~27 Torr and ~55 Torr, respectively. The steady-state pressure in the precursor manifolds was ~15 Torr and the pressure rise during the precursor exposures was ~1-2 Torr. The pressure downstream of the fluidized bed was measured with a separate Baratron capacitance manometer pressure gauge and was ~2 Torr. The overcoated sample was prepared using 5 cycles of Al<sub>2</sub>O<sub>3</sub> ALD over the mesoporous Pt/SiO<sub>2</sub> catalyst powder.

### **3. *Synthesis of 5cAl<sub>2</sub>O<sub>3</sub>/SiO<sub>2</sub> sample***

The same procedure described in section II.A.2 was used to overcoat 5 cycles of Al<sub>2</sub>O<sub>3</sub> ALD on 10 g of SiO<sub>2</sub>. The purpose for this sample is to study the Al<sub>2</sub>O<sub>3</sub> ALD behavior on the SiO<sub>2</sub> support in the absence of the Pt catalyst.

### **4. *Synthesis of 1cPd/Al<sub>2</sub>O<sub>3</sub> catalyst***

Al<sub>2</sub>O<sub>3</sub> powder (Sigma-Aldrich type CG-20, surface area: 118 m<sup>2</sup>/g, average pore volume: 0.26 cc/g, average pore size: 7.2 nm) was used as the catalyst support. 10 g of the Al<sub>2</sub>O<sub>3</sub> support was loaded into the Forge Nano Prometheus fluidized bed ALD reactor. The Pd ALD was performed at 200 °C and the N<sub>2</sub> flow rate was set to 80 sccm to fluidize the 10 g Al<sub>2</sub>O<sub>3</sub> powder as determined by visual observation through the glass window. The Pd ALD was performed using alternating exposures to 55 min of Pd(II) hexafluoroacetylacetonate (Pd(hfac)<sub>2</sub>, Sigma-Aldrich, 98%) and 40 min of formalin (37

wt% formaldehyde with 10-15 wt% methanol in H<sub>2</sub>O, Sigma-Aldrich) separated by 40 min purge times. These conditions were determined to be saturating using *in-situ* mass spectrometry measurements as will be described below. The formalin container was maintained at room temperature and the Pd(hfac)<sub>2</sub> bubbler was heated to 70 °C. Due to the low vapor pressure of Pd(hfac)<sub>2</sub>, the Pd precursor was supplied using a flow-through bubbler with 20 sccm ultrahigh purity N<sub>2</sub> supplied through a separate mass flow controller.

### 5. *Synthesis of 5cAl<sub>2</sub>O<sub>3</sub>/1cPd/Al<sub>2</sub>O<sub>3</sub> catalyst*

The same procedure described in section II.A.2 was used to overcoat 5 cycles of Al<sub>2</sub>O<sub>3</sub> ALD on 10 g of catalyst 1cPd/Al<sub>2</sub>O<sub>3</sub> with the exception of using 80 sccm carrier gas flow.

### **B. Characterization**

The ALD reaction products were monitored *in-situ* using a quadrupole mass spectrometer (QMS, Stanford Research Systems RGA300) housed in a differentially pumped chamber (50 L/s turbomolecular pump) connected to the ALD reactor outlet via a 50 μm aperture. N<sub>2</sub> physisorption analysis was performed at 77 K using a Micromeritics ASAP 2020 analyzer to characterize the specific surface area and porosity of the catalyst powders. The samples were degassed overnight at 250 °C prior to the measurements. Thermogravimetric analysis (TA Instruments, Discovery TGA 5500) was used to investigate the moisture loss. In the TGA experiments, ~15 mg of the sample was placed in a crucible. The crucible was heated from room temperature to 700 °C at a rate of 10 °C/min in ultra-high purity argon (99.999%) at a flow rate of 10 sccm. H<sub>2</sub> chemisorption was performed on the same Micromeritics analyzer using the double isotherm method. The samples were reduced in 2.8% H<sub>2</sub> at 500 °C and then re-oxidized at 40 °C. After flowing

helium, H<sub>2</sub> chemisorption was performed at 40 °C to generate the first isotherm, which yields the total amount of chemisorbed hydrogen. After flowing additional He, a second H<sub>2</sub> isotherm was generated at 40 °C providing the reversible bound chemisorbed hydrogen. The difference between the two isotherms gives the irreversible chemisorbed hydrogen on the Pt surface. The two isothermal curves were obtained in the 70-400 Torr pressure domain. Diffuse reflectance infrared Fourier transform spectroscopy (DRIFTS) measurements were performed using a Thermo Scientific Nicolet iS50 FTIR spectrometer equipped with an iS50 Automated Beam splitter exchanger (ABX). Samples were reduced in the measurement cell at 500 °C for 1 h in 2.8% H<sub>2</sub> and cooled to room temperature in He, then exposed to 1% CO for 15 min and purged with He for 5 min. The DRIFTS spectra were collected during the He flush. Calcination of the ALD overcoated samples for CO-DRIFTS was performed inside the measurement cell at 500 °C in air for 1 h. After purging with He for 20 min and reducing in 2.8% H<sub>2</sub> for 1h, the samples were cooled to room temperature and exposed to 1% CO for 15 min followed by a 5 min He purge. The DRIFTS spectra were collected during the He flush. X-ray photoelectron spectroscopy (XPS) measurements were performed on a Thermo Scientific K-Alpha+ spectrometer using a microfocused monochromatic Al K $\alpha$  (1487 eV) X-ray source. For charge compensation, a dual-beam electron flood gun (ultra-low energy coaxial electron and Ar<sup>+</sup> ion beam) was used. Low-resolution survey scans were performed in the energy range of 0-1300 eV and high-resolution XPS measurements were performed for the elements of interest. The adventitious C 1s peak (284.8 eV) was used for charge correction.

### **C. Catalytic Activity Measurement**

The propane dehydrogenation reaction was carried out at 600 °C under atmospheric pressure in a vertical quartz tubular reactor with a diameter of 10 mm. A thermocouple was inserted on top of the catalyst bed to monitor the reaction temperature. Approximately 600 mg of the catalysts were loaded for testing. To improve the temperature uniformity across the catalyst bed, 2 g of quartz sand (80 mesh size) was used to dilute the catalyst. The catalysts were reduced in 10% H<sub>2</sub> for 30 min at 500 °C before the catalytic activity measurement. The ALD overcoated catalysts were calcined in air at 500 °C for 1 h before the reduction. The reactant mixture consisted of 50/50 vol% of hydrogen (Airgas, 99.999%) and propane (Airgas, 99.5%) in down flow mode with a total flow of 130 sccm. The gas hourly space velocity (GHSV), defined as the volume flow rate of feed in ml/h divided by catalyst bed volume, is 3900 h<sup>-1</sup>. The concentration of the reactants and products was analyzed by an online gas chromatograph (Agilent, 6890 GC) equipped with a flame ionization detector (FID) and a thermal conductivity detector (TCD). The propane conversion and propylene selectivity were calculated as follows:

$$C_3H_8 \text{ conversion} = \frac{\text{moles of } C_3H_8 \text{ in} - \text{moles of } C_3H_8 \text{ out}}{\text{moles of } C_3H_8 \text{ in}} \times 100\% \text{ (Eq. 1)}$$

$$C_3H_6 \text{ selectivity} = \frac{3 \times \text{moles of } C_3H_6}{\text{moles of } (CH_4 + 2 \times C_2H_6 + 2 \times C_2H_4 + 3 \times C_3H_6 + 4 \times C_4 + 5 \times C_5 + 6 \times C_6)} \times 100\% \text{ (Eq. 2)}$$

2)

### III. Modeling

In order to understand the influence of the different experimental parameters on the fluidized bed ALD process, we have developed a model to predict the evolution with time of key observables including film thickness, precursor pressure in the downstream region,

and the concentration of vapor-phase reaction byproducts. Our model is based on three key assumptions:

- 1) Particles under fluidization mix much faster than the precursor saturation time. Under this approximation, we expect a narrow coverage distribution of the particles as, on average, all particles should receive an equal exposure.
- 2) Precursor transport and reaction inside the reactor can be modeled using average flows in the column under the plug flow approximation.
- 3) The ALD surface reactions follow irreversible first order Langmuir kinetics, a common approximation in the ALD literature.<sup>27</sup>

These three assumptions reduce the problem to a set of two differential equations for the precursor partial pressure inside the column and the growth kinetics of an average particle:

$$\bar{u} \frac{dp}{dz} = -\frac{S}{V} \bar{\beta} \frac{1}{4} v_{th} p \quad (\text{Eq. 3})$$

$$\frac{d\bar{\Theta}}{dt} = s_0 \frac{1}{4} v_{th} \frac{p}{k_B T} \beta_0 (1 - \bar{\Theta}) \quad (\text{Eq. 4})$$

In these equations,  $\bar{u}$  is the average flow velocity inside the column,  $p$  is the precursor partial pressure,  $z$  is the column height,  $S$  and  $V$  are the total surface area and the volume of the column, respectively,  $\bar{\beta} = \beta_0 (1 - \bar{\Theta})$  is the sticking coefficient where  $\beta_0$  is the sticking probability of the ALD process at zero coverage and  $\bar{\Theta}$  is the average fraction of surface sites reacted with the precursor,  $s_0$  is the average area of a single surface site,  $v_{th}$  is the mean thermal velocity, and  $k_B T$  is the product of the Boltzmann constant and the process temperature.<sup>28</sup>

This model can be solved analytically resulting in a solution that depends solely on two independent parameters: the Damköhler number,  $Da$ , which is a dimensionless number

typically used in chemical engineering defined as the ratio of precursor consumption rate to transport rate (in m<sup>3</sup>/s), and a characteristic saturation time,  $t_0$ , defined as the moles of reactive sites divided by the moles per second of precursor inserted in the reactor.

Eqs. 3 and 4 can be solved analytically for arbitrary pulse shapes. In the particular case of a square precursor pulse of partial pressure  $p_0$ , the resulting expressions for the average surface coverage and precursor partial pressure in the downstream region are:

$$\bar{\Theta} = 1 - \frac{1}{\text{Da}} \log \left( 1 + (e^{\text{Da}} - 1) e^{-\text{Da} \frac{t}{t_0}} \right) \quad (\text{Eq. 5})$$

$$p = \frac{p_0}{1 + (e^{\text{Da}} - 1) e^{-\text{Da} \frac{t}{t_0}}} \quad (\text{Eq. 6})$$

Here the values of Da and  $t_0$  are given by:

$$\text{Da} = \frac{S}{S_0} \frac{1}{4} \frac{v_{th} \bar{\beta}}{\bar{u}} \quad (\text{Eq. 7})$$

$$t_0 = \frac{S / (s_0 N_A)}{\text{moles per second}} \quad (\text{Eq. 8})$$

Where  $S_0$  is the cross-sectional area of the reactor and  $N_A$  is Avogadro's number.

Eqs. 5 and 6 allow us to predict the performance of ideal ALD processes in fluidized bed reactors similar to what it has been done in the past for cross-flow or spatial ALD processes.<sup>28</sup>

## IV. RESULTS AND DISCUSSION

### A. $\text{Al}_2\text{O}_3$ ALD

Our initial studies focused on characterizing the  $\text{Al}_2\text{O}_3$  ALD process in the fluidized bed reactor using pressure measurements and *in-situ* mass spectrometry. During the precursor dosing in the fluidized bed reactor, the partial pressures for TMA and  $\text{H}_2\text{O}$  were

~1.4 Torr and ~2.3 Torr, respectively (Figure 1). The amount of TMA dosed into the ALD reactor, which will be used to calculate the TMA utilization, can be estimated based on this TMA partial pressure. The TMA and H<sub>2</sub>O dose times required to saturate the 10 g Silicycle S10040M powder support (total surface area 940 m<sup>2</sup>) were 24 min and 13 min, respectively, based on *in-situ* mass spectrometry measurements as will be described below.

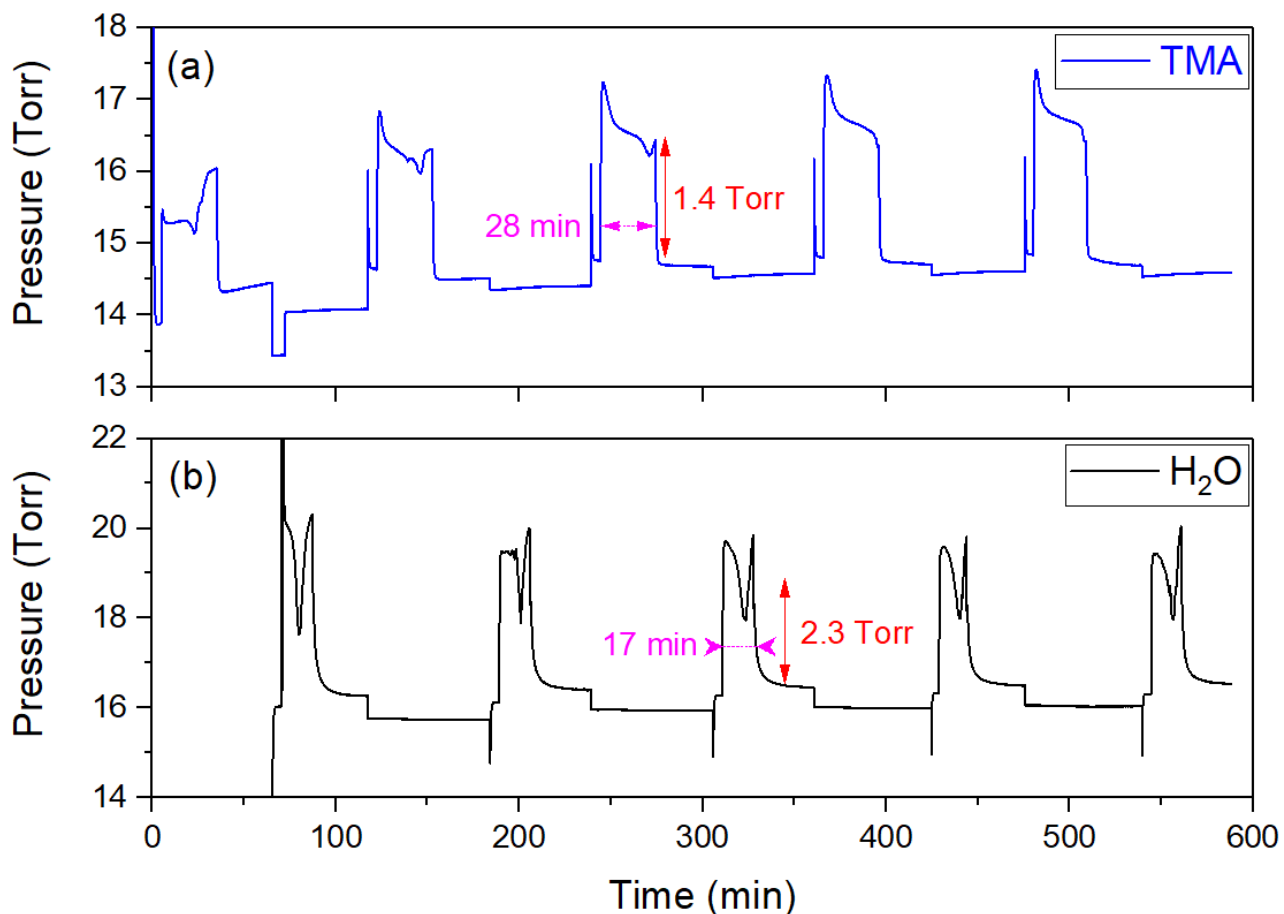


FIG. 1. Manifold pressures in the fluidized bed ALD reactor for (a) TMA and (b) H<sub>2</sub>O vs time during Al<sub>2</sub>O<sub>3</sub> ALD for the sample 5cAl<sub>2</sub>O<sub>3</sub>/SiO<sub>2</sub>.

Figure 2 shows the mass spectrometry data recorded during the synthesis of 5cAl<sub>2</sub>O<sub>3</sub>/SiO<sub>2</sub>. Figure 2 (a) shows the gas phase species monitored during the TMA dose. Species at  $m/z=16$  and  $m/z=15$  were detected during the TMA dose. According to previous studies of the Al<sub>2</sub>O<sub>3</sub> ALD reaction mechanism, CH<sub>4</sub> is formed when TMA reacts with the

hydroxylated (-OH) surface.<sup>29</sup> The mass spectrometer cracking pattern for methane in the literature shows that the  $m/z=15$   $\text{CH}_3$  fragment is  $\sim 90\%$  the intensity of the  $m/z=16$   $\text{CH}_4$  parent peak.<sup>30</sup> In agreement with the literature cracking pattern, the  $m/z=16$  and  $m/z=15$  peaks in Figure 2 (a) have the same shape and  $m/z=15$  peak has a slightly lower intensity compared to the  $m/z=16$  peak during the initial  $\sim 24$  minutes of the dose when the  $\text{CH}_4$  reaction product is formed. The breakthrough of TMA was observed after 24 min as signaled by the appearance of the  $m/z=57$  and  $m/z=72$  peaks which are attributed to the  $\text{Al}(\text{CH}_3)_2$  fragment of TMA and the parent compound, respectively.<sup>31</sup> It is interesting to note that, following the TMA saturation at  $\sim 24$  min, the  $m/z=15$  signal becomes higher than the  $m/z=16$  signal in Figure 2 (a). This is because the cracking pattern of TMA, unlike  $\text{CH}_4$ , exhibits a larger  $m/z=15$  peak compared to the  $m/z=16$  peak.<sup>32</sup> The increase in  $m/z=15$  relative to  $m/z=16$ , as well as the appearance of the  $m/z=57$  and  $m/z=72$  peaks at  $\sim 24$  min in Figure 2 (a), are all signatures of TMA breakthrough indicating saturation of the TMA surface reaction on the high surface area silica gel powder.

The mass spectrum recorded during the  $\text{H}_2\text{O}$  dose of the  $\text{Al}_2\text{O}_3$  ALD is shown in Figure 2 (b). The  $\text{CH}_4$  byproduct was detected immediately after initiating the  $\text{H}_2\text{O}$  dose due to the reaction between  $\text{H}_2\text{O}$  and surface  $-\text{Al}(\text{CH}_3)_2$  species as evidenced by the appearance of the  $m/z=16$  and  $m/z=15$  peaks in the expected ratio for  $\text{CH}_4$ . The  $m/z=16$  and  $m/z=15$  peak intensities dropped as the reaction proceeded indicating the consumption of reactive surface species. The breakthrough of  $\text{H}_2\text{O}$  ( $m/z=18$ ) was observed after  $\sim 13$  min at which point the  $m/z=16$  and  $m/z=15$  peaks decreased signaling the completion of the  $\text{H}_2\text{O}$  half reaction for the  $\text{Al}_2\text{O}_3$  ALD. The  $m/z=16$  peak persists for slightly longer compared to the  $m/z=15$  peak following the  $\text{H}_2\text{O}$  breakthrough in Figure 2 (b) since  $m/z=16$  is also a

crack of the H<sub>2</sub>O molecule. As shown in Figure 1, both TMA and H<sub>2</sub>O were intentionally overdosed by ~4 min to ensure completion of the surface reactions.

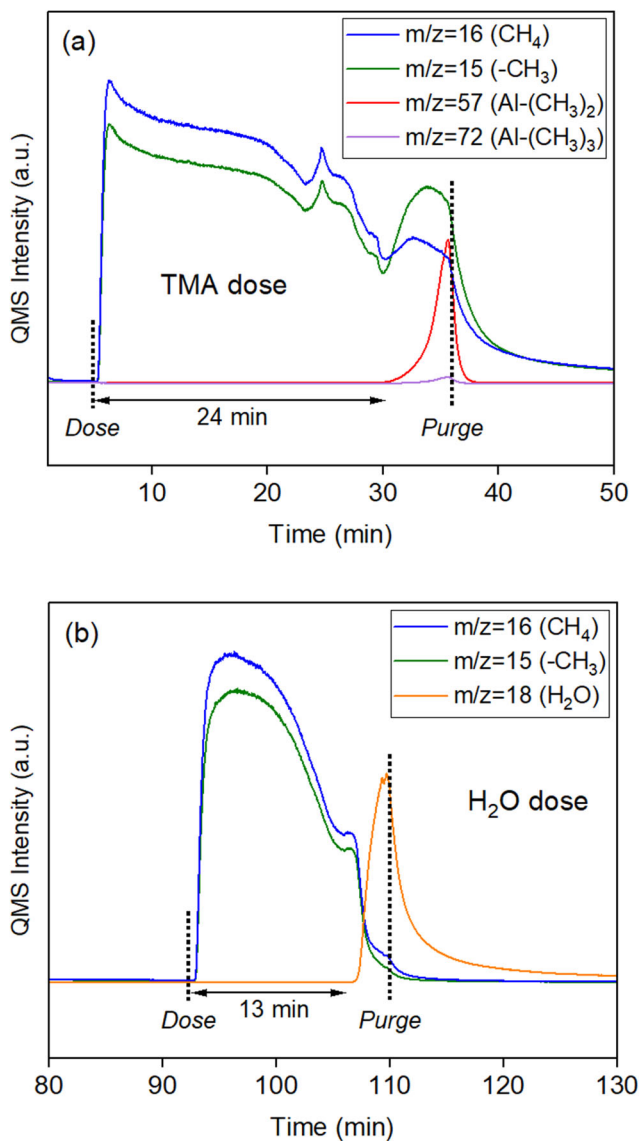


FIG. 2. *In-situ* mass spectrometry data recorded for one Al<sub>2</sub>O<sub>3</sub> ALD cycle during (a) TMA and (b) H<sub>2</sub>O doses on 10 g silica gel powder with a total surface area of 940 m<sup>2</sup>. The start of the precursor dose and purge steps are indicated by the vertical dashed lines.

The TMA precursor utilization,  $\Lambda_{\text{TMA}}$ , is defined as the amount of TMA required for saturation divided by the amount of TMA supplied. Based on the carrier gas flow rate (50 sccm), base pressure (14.5 Torr), and average partial pressure of TMA ( $1.6 \pm 0.3$  Torr),

the calculated flow rate of TMA is  $5.5 \pm 0.9$  sccm at  $40\text{ }^\circ\text{C}$  (TMA bottle temperature). Since the manifold temperature was  $100\text{ }^\circ\text{C}$ , the TMA flow rate was  $6.5 \pm 1.4$  sccm at this temperature. According to the study by Carlsson et al., the estimated fraction of TMA dimer under our conditions was 67%.<sup>33</sup> Thus, the total TMA supplied was calculated as  $0.0115 \pm 0.0020$  mol during the 24 min TMA dose. Assuming the density of  $\text{Al}_2\text{O}_3$  is 2.9 g/ml, the growth thickness after 1 cycle is  $2.0\text{ \AA}$ ,<sup>34, 35</sup> and the total surface area is  $940\text{ m}^2$  (surface area data was shown in Table 1, 10 g of  $\text{SiO}_2$  support was used), the product of those three numbers yields the estimated amount of  $\text{Al}_2\text{O}_3$  deposited, which is 0.55 g. Thus, the amount of TMA required for saturation is 0.0103 mol. The calculated  $\Lambda_{\text{TMA}}$  is  $91.8 \pm 14.6\%$ , suggesting that nearly all the TMA supplied reacted during the TMA dose with little waste. For comparison, our previous study of  $\text{Al}_2\text{O}_3$  ALD in a rotary drum reactor using  $1000\text{ m}^2$  powder yielded a lower precursor utilization of  $70\%$ <sup>20</sup>. However, our rotary drum ALD system measured a much shorter TMA saturation time of  $\sim 1.7$  min compared to 24 min in the present study for similar powder loadings. The much longer dose time in our fluidized bed reactor is due to the low carrier gas flow rate required to maintain a manifold pressure below the TMA vapor pressure and to achieve stable fluidization. The calculated flow rate of TMA into the fluidized bed reactor is  $4.28 \times 10^{-6}$  mol/s. In contrast, the TMA supply can be faster for the rotating drum by using much higher carrier gas flow rates. These higher TMA flow rates can be used without seriously impacting the precursor utilization due to the rapid rates of TMA surface reaction and diffusion.

We can compare these experimental results with predictions from our fluidized bed ALD model. In Figure 3 (a), we show the predicted evolution of surface coverage as a

function of time for various Damköhler numbers (Da), the ratio of precursor consumption to transport rate. As Da increases, the saturation time approaches  $t_0$ :

$$\Theta(t = t_0) \approx 1 - \frac{1}{\text{Da}} \log(2) \text{ (Eq. 9)}$$

This indicates that for higher Da, the process transitions from reaction limited to transport limited where the saturation time is dictated by the precursor supply rate. Under our experimental conditions, we calculate  $\text{Da} \sim 10^4$  for the TMA and H<sub>2</sub>O reactions indicating transport-limited behavior. In Figure 3 (b), we compare the predicted saturation dose times (lines) with the experimental saturation times for TMA and water (solid circles). The overall agreement is good, with the greatest uncertainty coming from estimating the precursor delivery rates which depend on the cross-sectional area of the inlet tubing at the position of the pressure gauges and the assumption that the pressure gauge signal can be integrated to determine the total number of moles. The two model curves in Figure 3 (b) represent the limits in the average area of a surface site required to satisfy an Al<sub>2</sub>O<sub>3</sub> stoichiometry. A key result from Figure 3 is that the slowdown in surface kinetics characteristic of self-limited processes does not significantly reduce throughput in a fluidized bed reactor: the model predicts a linear rise in surface coverage with time.

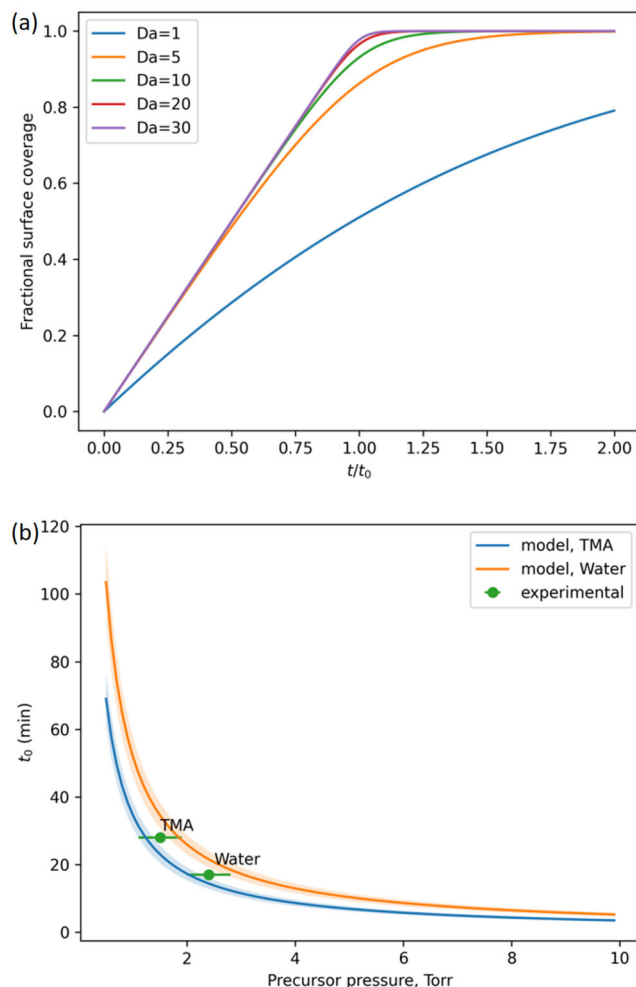


FIG. 3. (a) Evolution of average fractional surface coverage with time as predicted by the fluidized bed reactor ALD model for increasing values of the Damköhler number,  $Da$ . (b) Predicted dose times required to achieve saturation as a function of precursor pressure and comparison with experimental results presented in this work.

Figure 4 shows the normalized precursor partial pressure downstream of the fluidized bed as a function of time calculated from our model. For Damköhler number values  $Da > 5$ , the downstream precursor pressure is negligible until a “punch through” is observed at the saturation time,  $t_0$ . This behavior agrees well with the experimental results for both TMA and water (Figure 2) and indicates that ALD precursor utilization can be high in fluidized bed reactors, especially for chemistries that exhibit relatively high reactive

sticking coefficients such as TMA and H<sub>2</sub>O ( $\beta_0 \sim 10^{-4}$ ). Moreover, since Da is proportional to the powder substrate surface area, the punch-through transition becomes sharper and the precursor utilization increases for larger loadings of powder. This feature is attractive for scale-up and is most advantageous for high value precursors such as those used in noble metal ALD as will be discussed below.

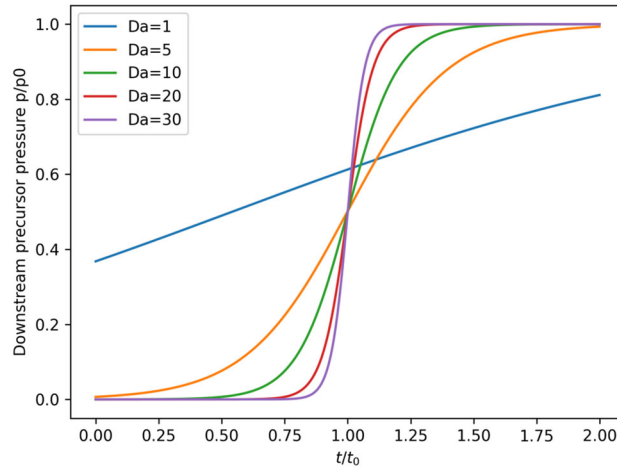


FIG. 4. Evolution of the precursor partial pressure downstream of the fluidized bed as a function of time for increasing values of the Damköhler number, Da. For  $Da > 5$ , the model predicts negligible precursor downstream until the precursor punches through. The punch-through time is the saturation time ( $t/t_0 = 1$ ), and the sharpness of the transition increases with Da which correlates with higher substrate surface areas.

Following these initial studies of the fluidized bed Al<sub>2</sub>O<sub>3</sub> ALD process, we performed measurements to characterize the Al<sub>2</sub>O<sub>3</sub> overcoated powders. N<sub>2</sub> physisorption analysis was performed to investigate the surface area and porosity changes after Pt impregnation, Pd ALD (discussed below), and Al<sub>2</sub>O<sub>3</sub> ALD overcoating. The adsorption-desorption isotherms shown in Figure 5 exhibit typical H4-type hysteresis for all the samples indicating the presence of mesopores. Table 1 summarizes the surface area, pore volume, and pore diameter deduced from the N<sub>2</sub> physisorption measurements. The changes

in these parameters upon Pt impregnation and Pd ALD are very small suggesting the formation of small nanoparticles for both the Pt and Pd. After 5 cycles of Al<sub>2</sub>O<sub>3</sub> ALD overcoating, the surface area decreased by 20% for both catalysts, from 94 m<sup>2</sup>/g to 75 m<sup>2</sup>/g for the Pt/SiO<sub>2</sub> and from 118 m<sup>2</sup>/g to 94 m<sup>2</sup>/g for the 1cPd/Al<sub>2</sub>O<sub>3</sub>. The pore volumes and pore diameters also decreased following the Al<sub>2</sub>O<sub>3</sub> ALD overcoating. The average pore diameter decreased from 28.9 nm for the Pt/SiO<sub>2</sub> sample to 22.6 nm for the 5cAl<sub>2</sub>O<sub>3</sub>/Pt/SiO<sub>2</sub> sample. This is a change of 6.3 nm which is larger than the expected change of 4 nm based on the 0.2 nm Al<sub>2</sub>O<sub>3</sub> growth per cycle and may indicate some Al<sub>2</sub>O<sub>3</sub> CVD due to residual H<sub>2</sub>O. Elongating the purge time after the H<sub>2</sub>O dose could minimize the Al<sub>2</sub>O<sub>3</sub> CVD. Alternatively, performing the Al<sub>2</sub>O<sub>3</sub> ALD at a higher temperature (but below the TMA decomposition temperature), or elevating the temperature during the H<sub>2</sub>O purge step would minimize the Al<sub>2</sub>O<sub>3</sub> CVD. We note that the 20% decrease in surface area for the 5cAl<sub>2</sub>O<sub>3</sub>/Pt/SiO<sub>2</sub> sample is larger than our previous surface area measurements for ALD Al<sub>2</sub>O<sub>3</sub> on S10040M silica gel powders,<sup>16</sup> and this also suggests some Al<sub>2</sub>O<sub>3</sub> CVD. In contrast, the average pore diameter only decreased by 0.3 nm for the 5cAl<sub>2</sub>O<sub>3</sub>/1cPd/Al<sub>2</sub>O<sub>3</sub> sample compared to the 1cPd/Al<sub>2</sub>O<sub>3</sub> sample suggesting that the very small mesopores do not become conformally coated by the Al<sub>2</sub>O<sub>3</sub> ALD for this substrate. It is possible that some of the internal porosity is accessible to the N<sub>2</sub> molecules used for the physisorption analysis but not for the larger TMA molecules used for the Al<sub>2</sub>O<sub>3</sub> ALD. The moisture content retained inside the pores of SiO<sub>2</sub> and 5cAl<sub>2</sub>O<sub>3</sub>/SiO<sub>2</sub> was measured by TGA. The samples were heated from room temperature to 700 °C and the moisture loss was 5.5% and 3.7% for the SiO<sub>2</sub> and 5cAl<sub>2</sub>O<sub>3</sub>/SiO<sub>2</sub> samples, respectively. The smaller weight change for

the 5cAl<sub>2</sub>O<sub>3</sub>/SiO<sub>2</sub> is expected based on the lower surface area of this sample as determined by the N<sub>2</sub> physisorption analysis.

TABLE 1. N<sub>2</sub> physisorption analysis results

Sample	Surface area (m <sup>2</sup> /g)	Average pore volume (cc/g)	Average pore diameter (nm)
SiO <sub>2</sub>	93.7	0.72	27.6
Pt/SiO <sub>2</sub>	100.5	0.69	28.9
5cAl <sub>2</sub> O <sub>3</sub> /Pt/SiO <sub>2</sub>	75.1	0.56	22.6
Al <sub>2</sub> O <sub>3</sub>	118.4	0.26	7.2
1cPd/Al <sub>2</sub> O <sub>3</sub>	120.3	0.24	6.3
5cAl <sub>2</sub> O <sub>3</sub> /1cPd/Al <sub>2</sub> O <sub>3</sub>	93.7	0.17	6.0

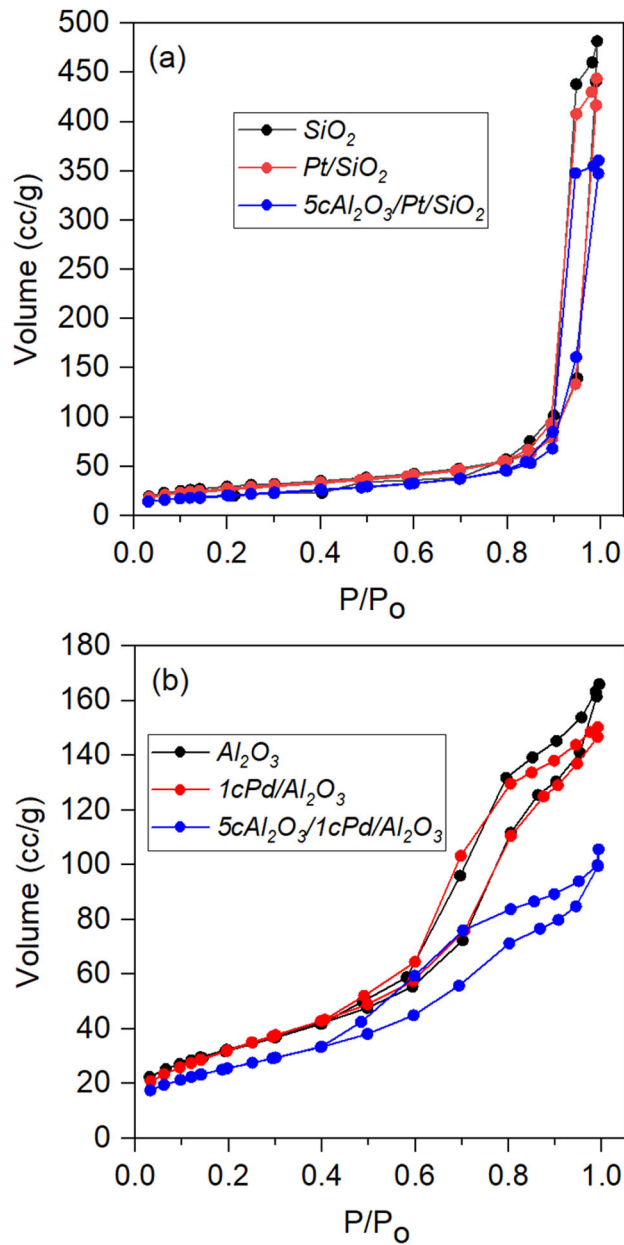


FIG. 5. N<sub>2</sub> adsorption-desorption isotherms for (a) 5cAl<sub>2</sub>O<sub>3</sub>/1cPt/SiO<sub>2</sub> and (b) 5cAl<sub>2</sub>O<sub>3</sub>/1cPd/Al<sub>2</sub>O<sub>3</sub>. Black traces show data for bare substrate, red traces are following metal ALD, and blue traces are following 5c Al<sub>2</sub>O<sub>3</sub> ALD overcoating.

The surface elemental composition of the 5cAl<sub>2</sub>O<sub>3</sub>/SiO<sub>2</sub>, 5cAl<sub>2</sub>O<sub>3</sub>/Pt/SiO<sub>2</sub>, Pt/SiO<sub>2</sub>, and 1cPd/Al<sub>2</sub>O<sub>3</sub> samples were examined using XPS measurements and the results are shown in Figure 6. The Al 2p spectra were fit to two symmetric peaks at 73.4 eV and at 74.8 eV for both 5cAl<sub>2</sub>O<sub>3</sub>/SiO<sub>2</sub> and 5cAl<sub>2</sub>O<sub>3</sub>/Pt/SiO<sub>2</sub> in Figure 6 (a) and (b), which are

assigned to Al-O and Al-OH, respectively. These results are similar to the study by Smyntyna et al. on Al<sub>2</sub>O<sub>3</sub> ALD coated porous silicon.<sup>36</sup> Next, the Pt 4f spectrum for sample Pt/SiO<sub>2</sub> (Figure 6 (c)) was deconvoluted as two doublet peaks at 71.3 eV and 72.8 eV, which can be ascribed to Pt metal and PtO, respectively.<sup>37</sup> Since Pt was impregnated using H<sub>2</sub>PtCl<sub>6</sub>, a high resolution Cl 2p XPS scan was performed (Figure 6 (d)). The measured Cl content is 0.4 at%. This low chlorine content is desirable for catalytic applications since chlorine has an inhibiting effect on catalytic reactions.<sup>38</sup> For sample 1cPd/Al<sub>2</sub>O<sub>3</sub>, the Pd 3d spectrum (Figure 6 (e)) was deconvoluted into five peaks where the highest binding energy peak at 346.6 eV is due to plasmons. The peaks at 335.2 eV and 340.5 eV correspond to the crystal field split Pd 3d<sub>5/2</sub> and 3d<sub>3/2</sub> peaks of metallic Pd, whereas the higher energy doublet peaks at 337.2 eV (Pd3d<sub>5/2</sub>) and 342.5 eV (Pd 3d<sub>3/2</sub>) correspond to PdO.<sup>39, 40</sup> Clearly, the presence of Pd in multiple oxidation states is observed in the 1cPd/Al<sub>2</sub>O<sub>3</sub> sample. After deconvolution, the F 1s spectrum (Figure 6(f)) contains a peak at 687.5 eV, which is assigned to C-F from the -hfac ligands. There is another peak at 684.5 eV, which has been previously assigned to Al-F.<sup>41</sup> The presence of Al-F suggests the readsorption of -hfac ligands on the Al<sub>2</sub>O<sub>3</sub> surface, which will be discussed later.

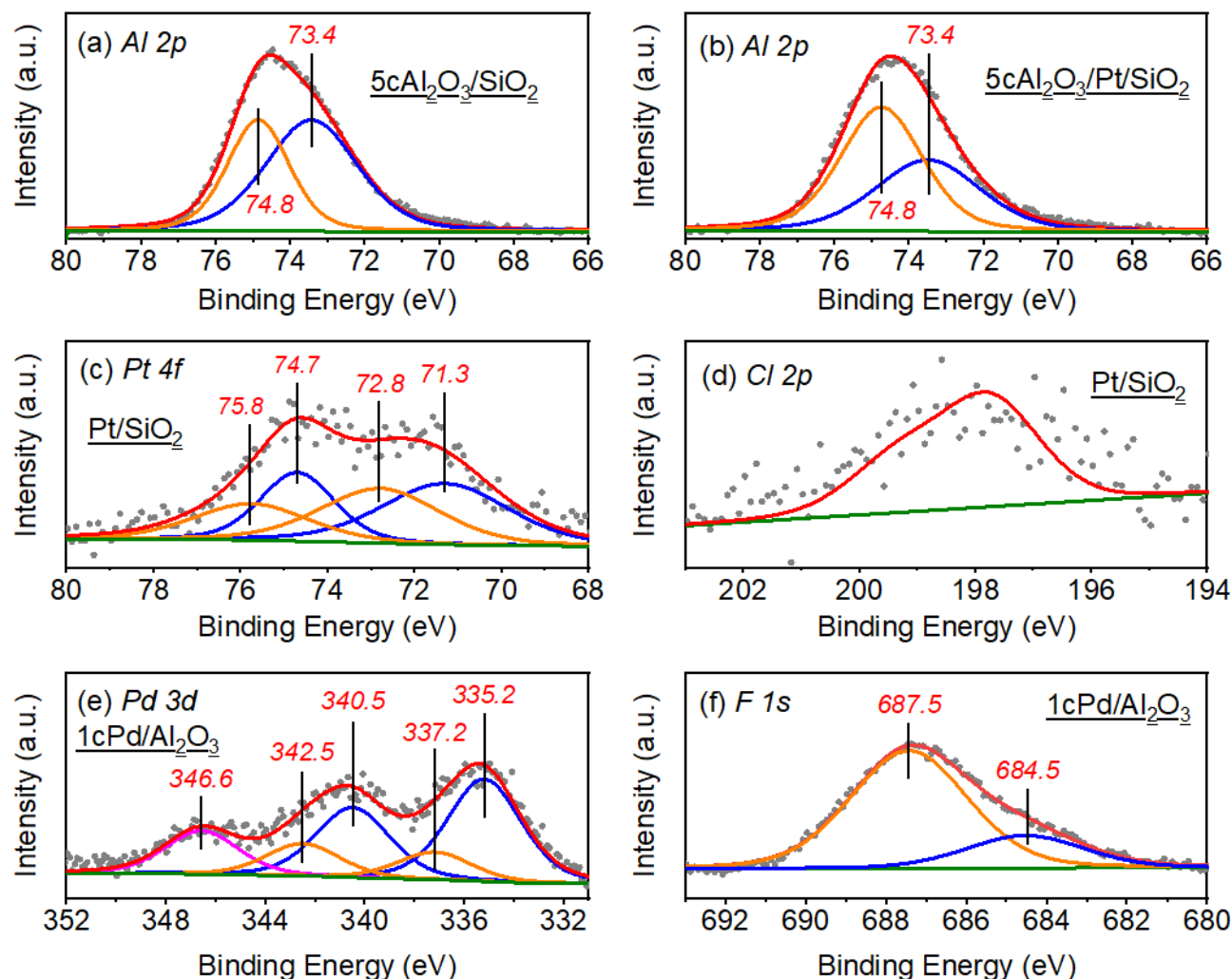


FIG. 6. XPS spectra at Al 2p core level for sample (a)  $5c\text{Al}_2\text{O}_3/\text{SiO}_2$  and (b)  $5c\text{Al}_2\text{O}_3/\text{Pt}/\text{SiO}_2$ ; XPS spectra at (c) Pt 4f and (d) Cl 2p core levels for sample  $\text{Pt}/\text{SiO}_2$ ; XPS spectra at (e) Pd 3d and (f) F 1s core levels for sample  $1c\text{Pd}/\text{Al}_2\text{O}_3$ .

CO-DRIFTS and  $\text{H}_2$  chemisorption measurements were performed to evaluate the accessibility of the Pt atoms. The DRIFTS spectra following CO chemisorption are shown in Figure 7 (a). The peak around  $2090\text{ cm}^{-1}$  was assigned to CO bonded on relatively large Pt nanoparticles and the shoulder around  $2074\text{ cm}^{-1}$  was assigned to CO bonded on relatively small Pt nanoparticles.<sup>42</sup> The intensity of both features for the fresh  $\text{Pt}/\text{SiO}_2$  catalyst decreased after five cycles of  $\text{Al}_2\text{O}_3$  ALD overcoating suggesting that the Pt nanoparticles were partially covered by the  $\text{Al}_2\text{O}_3$  ALD. The CO IR-DRIFTS absorption

signal increases following calcination of the 5cAl<sub>2</sub>O<sub>3</sub>/Pt/SiO<sub>2</sub> sample suggesting more Pt atoms were exposed, which we attribute to the creation of nanopores in the Al<sub>2</sub>O<sub>3</sub> overcoat that form when the coating densifies upon heating.<sup>8, 43, 44</sup> The purpose for the calcination is to re-expose more Pt atoms after the ALD overcoating, since only the exposed surfaces of the Pt nanoparticles are catalytically active. The amount of exposed Pt atoms was quantified using H<sub>2</sub> chemisorption. Similar to the CO-DRIFTS results, the chemisorbed H<sub>2</sub> on the Pt surface decreased from 3.24 to 2.04 μmol/g after 5 cycles of Al<sub>2</sub>O<sub>3</sub> ALD overcoating and increased to 2.65 μmol/g after calcination in air, implying that 81% of the surface Pt sites were still available for catalysis. Based on the H<sub>2</sub> chemisorption measurements, the Pt dispersion is 42% and the average Pt nanoparticle size is 3.3 nm.<sup>45</sup> The H<sub>2</sub> chemisorption analysis cannot be used to estimate the particle size for the catalyst after ALD overcoating since the change in chemisorbed H<sub>2</sub> is no longer solely from the change in nanoparticle size but also from the Al<sub>2</sub>O<sub>3</sub> overcoat covering the surface Pt atoms. However, the Pt/SiO<sub>2</sub> catalyst in this study was calcined at 500 °C before the ALD overcoating, and we assume the Pt nanoparticles size remains unchanged during the Al<sub>2</sub>O<sub>3</sub> ALD since the Al<sub>2</sub>O<sub>3</sub> ALD was performed at the much lower temperature of 200 °C.

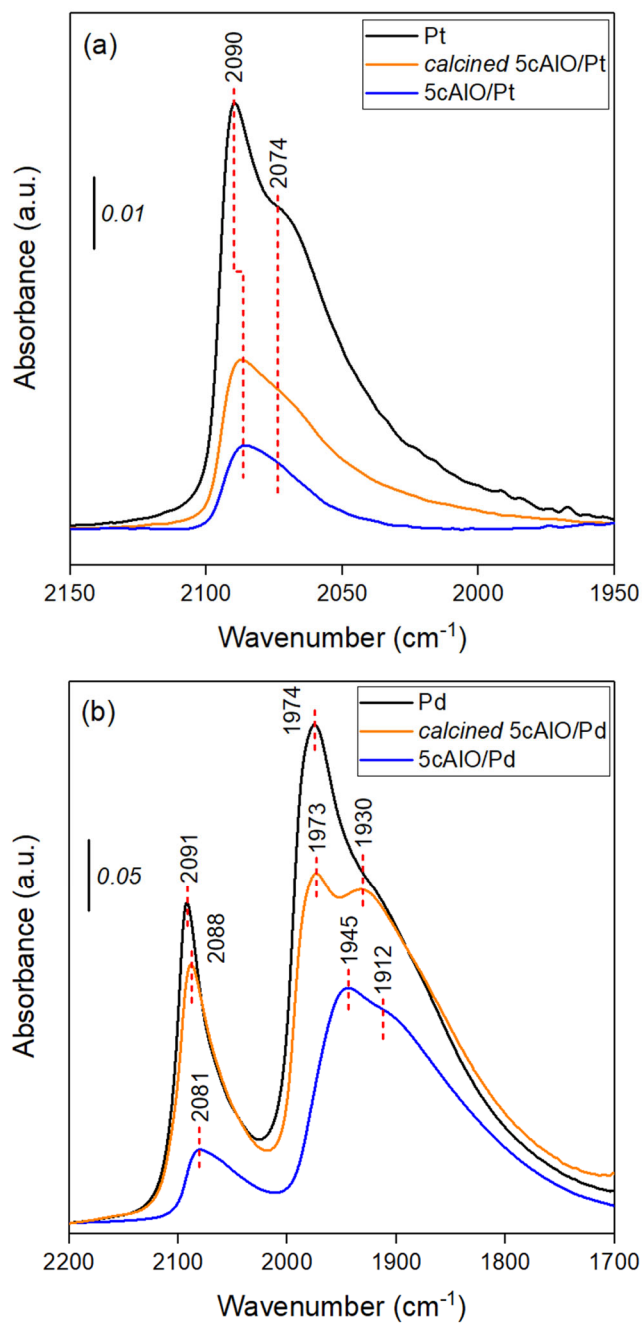


FIG. 7. DRIFTS measurements following CO adsorption on (a) Pt and (b) Pd catalysts. Black lines show the initial catalyst, blue lines are following 5 cycles of Al<sub>2</sub>O<sub>3</sub> ALD overcoat, and orange lines are after calcination for 1 hour at 500 °C in air.

The performance of both the Pt/SiO<sub>2</sub> and 5cAl<sub>2</sub>O<sub>3</sub>/Pt/SiO<sub>2</sub> catalysts were evaluated using the propane dehydrogenation reaction and the results are shown in Figure 8 (a). It is evident from Figure 8 (a) that the uncoated Pt/SiO<sub>2</sub> catalyst deactivated dramatically since

the propane conversion dropped from 10.5% to 3.9% after 20 h under reaction conditions. In contrast, the 5cAl<sub>2</sub>O<sub>3</sub>/Pt/SiO<sub>2</sub> catalyst was much more stable and the propane conversion decreased only slightly from 9.2% to 7.8%. During the 20 h reaction, the propylene selectivity remained almost unchanged at 91.2±1.1% for the ALD overcoated catalyst. However, the propylene selectivity dropped from 94.4% to 87.7% as the reaction proceeded for the uncoated catalyst. According to previous studies, ALD Al<sub>2</sub>O<sub>3</sub> preferentially binds to the undercoordinated edge and corner sites of Pt nanoparticles, which are the sites most likely to form coking species and deactivate.<sup>46,47</sup> Thus, overcoating these sites with ALD Al<sub>2</sub>O<sub>3</sub> reduces the coking propensity. Al<sub>2</sub>O<sub>3</sub> overcoats also form a physical barrier that prevents Pt nanoparticles from sintering during catalysis. Previous studies have shown that more surface Pt sites (both undercoordinated and terrace sites) are preserved for ALD overcoated catalysts due to the persistence of smaller Pt nanoparticles which enhances the catalyst activity and longevity.<sup>9</sup>

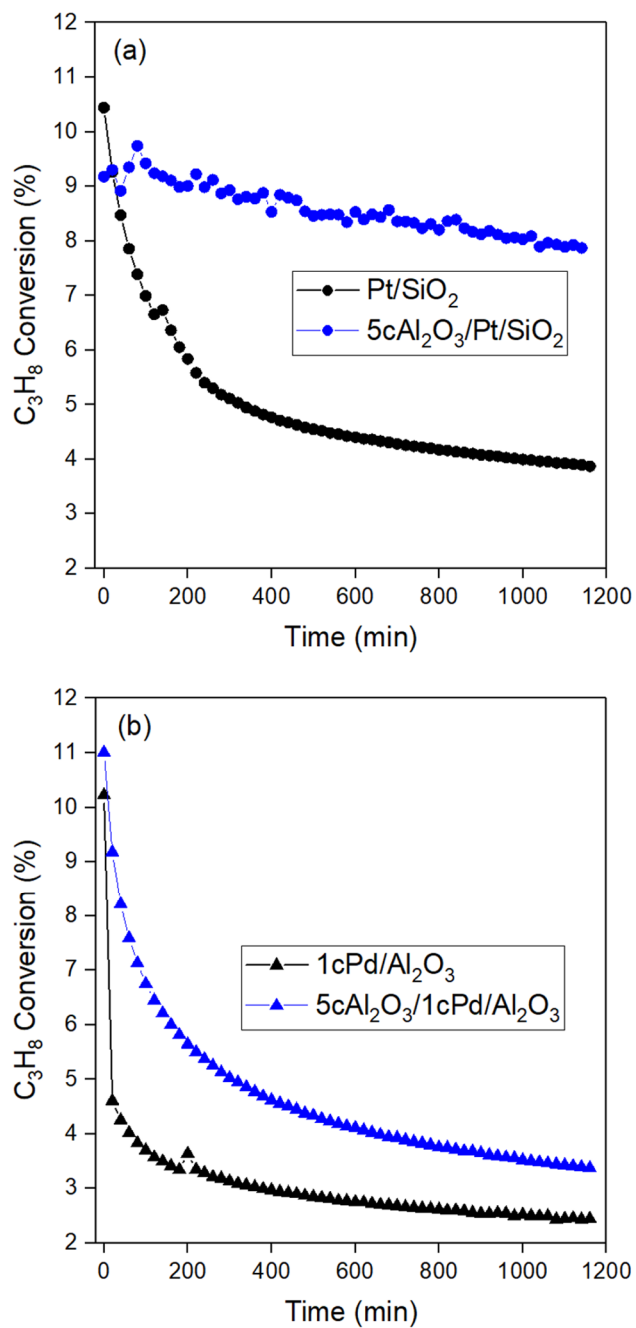
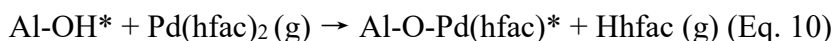


FIG. 8. Time-on-stream propane conversion for (a) Pt and (b) Pd catalysts. Black symbols show conversion measurements for the bare catalysts and blue symbols show conversion data for the ALD overcoated catalysts.

## B. Pd ALD

Next, we synthesized Pd catalysts using one cycle of Pd(hfac)<sub>2</sub>/HCHO for Pd ALD on the Al<sub>2</sub>O<sub>3</sub> powder substrate. The Pd nanoparticle size has been shown to increase with ALD Pd cycles, so one ALD Pd cycle was used to produce the smallest Pd nanoparticles.<sup>48</sup> We performed *in-situ* mass spectroscopy measurements during the Pd(hfac)<sub>2</sub> and HCHO exposures and the results are shown in Figure 9. During the Pd(hfac)<sub>2</sub> dose, signals at m/z=44 and m/z=69 were monitored but no significant changes in these signals were detected until 55 min after the beginning of the Pd(hfac)<sub>2</sub> exposure at which point both signals increased and persisted until the end of the Pd(hfac)<sub>2</sub> exposure (Figure 9 (a)). We assign the m/z=69 to -CF<sub>3</sub>. This is the largest peak in the cracking pattern for hexafluoroacetylacetone (Hhfac) and is also a prominent peak in the cracking pattern for Pd(hfac)<sub>2</sub>.<sup>49</sup> The origin of the m/z=44 signal is unclear as this peak is very small in the cracking pattern for Hhfac. However, we observed both m/z=69 and m/z=44 when Pd(hfac)<sub>2</sub> was dosed into an empty reactor implying that they are both indicative of Pd(hfac)<sub>2</sub> in our ALD system. We tentatively assign the m/z=44 peak to CO<sub>2</sub> and note that this peak was observed previously during *in-situ* QMS measurements of Pd ALD.<sup>50</sup>

The surface reaction during the Pd(hfac)<sub>2</sub> exposure on the Al<sub>2</sub>O<sub>3</sub> powder surface is likely to be:



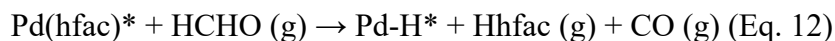
where the asterisks designate surface species.<sup>51</sup> From Eq. 10, we expect that the m/z=69 signal should appear immediately after the Pd(hfac)<sub>2</sub> dose and persist until the precursor is shut off since this peak is a crack of both the Pd(hfac)<sub>2</sub> precursor and the Hhfac product. The fact that no m/z=69 signal was observed until 55 min after the Pd(hfac)<sub>2</sub> dose suggests that the Hhfac product readsorbed on the Al<sub>2</sub>O<sub>3</sub> surface and this readsorption persisted until

all the surface sites were occupied. The -hfac ligands adsorbed on the Al<sub>2</sub>O<sub>3</sub> surface would block the adsorption of Pd(hfac)<sub>2</sub> in this ALD cycle. George et al. discovered that Hhfac readsorbs on Al<sub>2</sub>O<sub>3</sub> through reaction with surface -OH groups to form Al(hfac)\* species according to:<sup>52</sup>



In summary, we attribute the appearance of m/z=69 and m/z=44 signals after 55 min in Figure 9 (a) to the breakthrough of Pd(hfac)<sub>2</sub> following saturation of Eqs. 10 and 11.

Figure 9 (b) shows the QMS data recorded during the HCHO exposure. The surface reaction during the HCHO exposure for Pd ALD is believed to be:<sup>51</sup>



Signals were detected immediately for m/z=69 and m/z=44 upon initiating the HCHO exposure and these signals persist until the HCHO is turned off. In addition, the m/z=69 signal rises to a maximum at ~77 min and then decreases steadily until the purge begins at ~92 min. The m/z=44 shows similar behavior although the trend is less clear due to the larger baseline. These results support our hypothesis that the m/z=69 and m/z=44 signals derive from the Hhfac product.

There is a slight delay between the start of the HCHO exposure and the appearance of signal at m/z=30, one of the strongest peaks for HCHO.<sup>53</sup> This phenomenon has been observed previously, which is probably due to a very slow reaction rate of HCHO to remove the hfac ligands.<sup>50</sup> If the HCHO reaction rate is sufficiently slow on the Pd(hfac)\* terminated surface, then the concentration of HCHO vapor in the reactor will not be

reduced significantly during the reaction and the HCHO peak will be observed continuously throughout the dose. The HCHO dose was turned off for 6 min between ~92 and 98 min (marked as “purge” and “dose” in Figure 9 (b)). During this time, the  $m/z=30$ ,  $m/z=69$  and  $m/z=44$  signals all decreased. However, when the HCHO dose was turned on again at ~98 min, the  $m/z=69$  signals increased to a much smaller level than during the start of the HCHO dose at ~77 min. The  $m/z=69$  and  $m/z=44$  signals are not part of the HCHO cracking pattern,<sup>53</sup> and we attribute these persistent signals to the reaction of HCHO with Pd(hfac)\* species on the walls of the mass spectrometer vacuum chamber. In summary, we believe that the peak in the  $m/z=69$  signal at ~77 min is the most reliable metric to monitor saturation of the HCHO reaction on the Al<sub>2</sub>O<sub>3</sub> powder during the Pd ALD. The XPS measurements in Figure 6 (f) suggest the existence of fluorine impurities after 1 cycle of Pd ALD. These impurities may hinder precursor adsorption during the following Al<sub>2</sub>O<sub>3</sub> ALD thereby reducing the Al<sub>2</sub>O<sub>3</sub> growth per cycle.

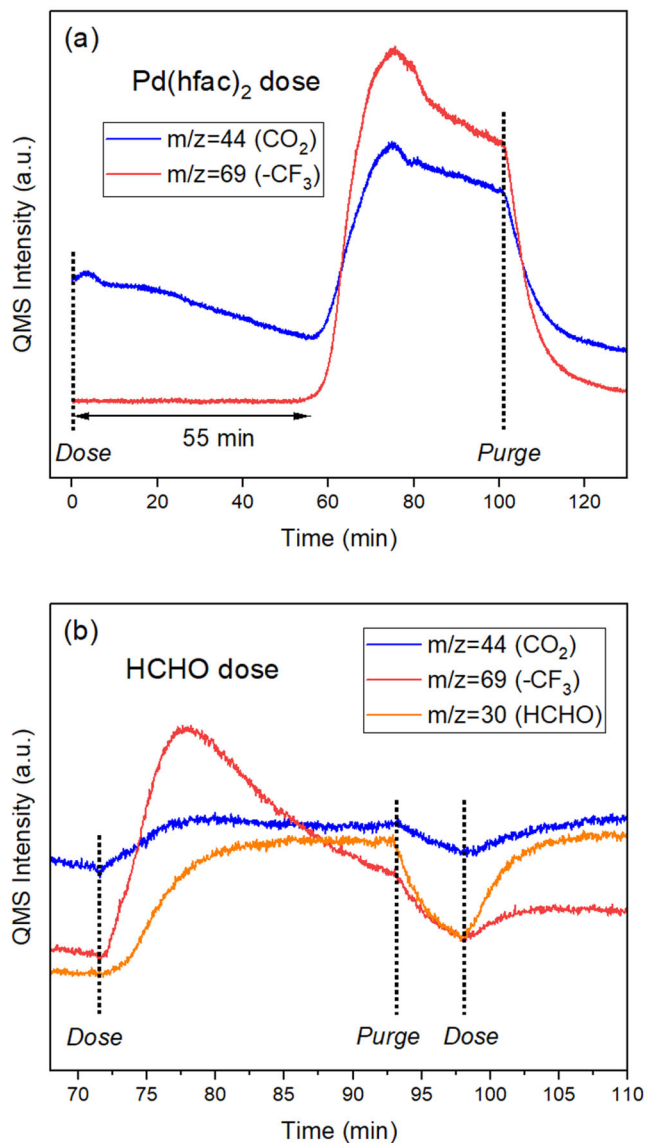


FIG. 9. Mass spectrometry data of one Pd ALD cycle during (a) Pd(hfac)<sub>2</sub> and (b) HCHO dose.

After synthesizing the Pd catalysts, we performed DRIFTS measurements of CO chemisorption (Figure 7 (b)). Three CO vibrational bands at 2090, 1974, and 1930 cm<sup>-1</sup> are observed, which can be assigned to linear-adsorbed CO on (111) facets of Pd particles, bridge-adsorbed CO on undercoordinated sites and facets other than the (111) facets of Pd particles, and bridge-adsorbed CO on the (111) facets of Pd particles, respectively.<sup>54</sup>

Similar to the Pt catalysts, the intensity of all three bands for the fresh 1cPd/Al<sub>2</sub>O<sub>3</sub> catalyst decreased after five cycles of Al<sub>2</sub>O<sub>3</sub> ALD overcoat suggesting that the Pd nanoparticles were partially covered by the Al<sub>2</sub>O<sub>3</sub> ALD. The IR intensity was partially restored upon calcination indicating the formation of nanopores in the overcoated Al<sub>2</sub>O<sub>3</sub> layer exposing new Pd surfaces.<sup>43,44</sup> For the uncoated Pd catalyst, the peak at 1974 cm<sup>-1</sup> was much stronger than the peak at 1930 cm<sup>-1</sup>. However, the intensities of both peaks were similar after ALD overcoating and calcination suggesting the Al<sub>2</sub>O<sub>3</sub> deposited preferentially at corners, steps, and edges of the Pd nanoparticles while leaving the catalytically active Pd (111) facets accessible. This phenomenon indicates that Al<sub>2</sub>O<sub>3</sub> ALD initiates nonuniformly on the Pd surface which may decrease the Al<sub>2</sub>O<sub>3</sub> ALD growth per cycle.

The performance of the Pd catalysts without and with ALD overcoat was evaluated using the propane dehydrogenation reaction as shown in Figure 8 (b). The propane conversion for the uncoated Pd catalyst dropped significantly from 10.2% to 4.6% within the first 20 min and further decreased to 2.4% after 20 h due to rapid coke formation and Pd nanoparticle sintering. With 5 cycles of Al<sub>2</sub>O<sub>3</sub> ALD overcoat, the catalyst still deactivated but at a much slower rate, from 11.0% to 3.3% after 20 h under reaction condition. The overcoated Pd catalyst maintained a higher propane conversion suggesting more active Pd sites were preserved possibly due to less coke formed and the retention of smaller Pd nanoparticles.

## V. CONCLUSION

In this work, fluidized bed ALD was applied to prepare overcoated catalysts on decagram quantities of powder substrates. The chemistry and saturation for both Al<sub>2</sub>O<sub>3</sub> and Pd ALD were studied by *in-situ* mass spectrometry. The breakthrough of TMA and H<sub>2</sub>O

was used as an indicator for reaction saturation during the Al<sub>2</sub>O<sub>3</sub> ALD and the TMA precursor utilization was 91.8±14.6%. We believe this is the first study comparing *in-situ* measurements with analytical predictions of precursor saturation. The predicated saturation time from our modeling match well with the experimental results and the precursor utilization of ALD under a fluidized reactor configuration is very high. In the Pd ALD study, the absence of -hfac ligands after the initial Pd(hfac)<sub>2</sub> dose was observed, which suggests the -hfac ligands could readsorb on Al<sub>2</sub>O<sub>3</sub> surface until all the surface sites were occupied with the yield of both Pd(hfac)\* and Al(hfac)\* surface species. Propane dehydrogenation was used as a probe reaction for the Pt and Pd catalysts. It was demonstrated that the activity for both catalysts was significantly improved after Al<sub>2</sub>O<sub>3</sub> ALD overcoating, confirming the ability of fluidized ALD to synthesize active and stable powder catalysts.

## ACKNOWLEDGEMENTS

The submitted manuscript has been created by UChicago Argonne, LLC, Operator of Argonne National Laboratory (“Argonne”). Argonne, a U.S. Department of Energy (DOE) Office of Science laboratory, is operated under Contract No. DE-AC02-06CH11357. This work was funded by the Argonne Laboratory Directed Research and Development (LDRD) program.

## AUTHOR DECLARATIONS

### Conflict of Interest

The Authors have no conflicts to disclose.

## DATA AVAILABILITY STATEMENT

The data that supports the findings of this study are available within the article.

## REFERENCES

- <sup>1</sup>S. M. George, *Chem. Rev.* **110**, 111 (2010).
- <sup>2</sup>R. W. Johnson, A. Hultqvist, and S. F. Bent, *Mater. Today* **17**, 236 (2014).
- <sup>3</sup>H. Kim, H. B. R. Lee, and W. J. Maeng, *Thin Solid Films* **517**, 2563 (2008).
- <sup>4</sup>Y. Lei, B. Liu, J. Lu, R. J. Lobo-Lapidus, T. Wu, H. Feng, X. Xia, A. U. Mane, J. A. Libera, J. P. Greeley, J. T. Miller, and J. W. Elam, *Chem. Mater.* **24**, 3525 (2012).
- <sup>5</sup>K. Cao, Q. Zhu, B. Shan, and R. Chen, *Sci. Rep.* **5**, 8470 (2015).
- <sup>6</sup>M. Piernavieja-Hermida, Z. Lu, A. White, K.-B. Low, T. Wu, J. W. Elam, Z. Wu, and Y. Lei, *Nanoscale* **8**, 15348 (2016).
- <sup>7</sup>S. Sun, G. Zhang, N. Gauquelin, N. Chen, J. Zhou, S. Yang, W. Chen, X. Meng, D. Geng, M. N. Banis, R. Li, S. Ye, S. Knights, G. A. Botton, T.-K. Sham, and X. Sun, *Sci. Rep.* **3**, 1775 (2013).
- <sup>8</sup>J. Lu, B. Fu, M. C. Kung, G. Xiao, J. W. Elam, H. H. Kung, and P. C. Stair, *Science* **335**, 1205 (2012).
- <sup>9</sup>H. Feng, J. Lu, P. C. Stair, and J. W. Elam, *Catal. Lett.* **141**, 512 (2011).

- <sup>10</sup>Z. Lu and J. W. Elam, "Synthesis Techniques for Ultrathin Oxide Layers of Heterogeneous Catalysts" in *Ultrathin Oxide Layers for Solar and Electrocatalytic Systems*, edited by H. Frei and D. V. Esposito, (The Royal Society of Chemistry, Croydon, UK, 2022).
- <sup>11</sup>Z. Lu, R. W. Tracy, M. Leigh Abrams, N. L. Nicholls, P. T. Barger, T. Li, P. C. Stair, A. A. Dameron, C. P. Nicholas, and C. L. Marshall, *ACS Catal.* **10**, 13957 (2020).
- <sup>12</sup>Z. Lu, X. Liu, B. Zhang, Z. Gan, S. Tang, L. Ma, T. Wu, G. J. Nelson, Y. Qin, C. H. Turner, and Y. Lei, *J. Catal.* **377**, 419 (2019).
- <sup>13</sup>E. Sarnello, Z. Lu, S. Seifert, R. E. Winans, and T. Li, *ACS Catal.* **11**, 2605 (2021).
- <sup>14</sup>Z. Lu, O. Kizikaya, A. J. Kropf, M. Piernavieja-Hermida, J. T. Miller, R. Kurtz, J. W. Elam, and Y. Lei, *Catal. Sci. Tech.* **6**, 6845 (2016).
- <sup>15</sup>J. A. Libera, J. W. Elam, and M. J. Pellin, *Thin Solid Films* **516**, 6158 (2008).
- <sup>16</sup>J. W. Elam, J. A. Libera, T. H. Huynh, H. Feng, and M. J. Pellin, *J. Phys. Chem. C* **114**, 17286 (2010).
- <sup>17</sup>Z. Lu, M. Piernavieja-Hermida, C. H. Turner, Z. Wu, and Y. Lei, *J. Phys. Chem. C* **122**, 1688 (2018).
- <sup>18</sup>J. W. Elam, D. Routkevitch, P. P. Mardilovich, and S. M. George, *Chem. Mater.* **15**, 3507 (2003).
- <sup>19</sup>J. A. McCormick, B. L. Cloutier, A. W. Weimer, and S. M. George, *J. Vac. Sci. Technol. A* **25**, 67 (2007).
- <sup>20</sup>M. W. Coile, M. J. Young, J. A. Libera, A. U. Mane, and J. W. Elam, *J. Vac. Sci. Technol. A* **38**, 52403 (2020).

- <sup>21</sup>P. Poodt, A. Lankhorst, F. Roozeboom, K. Spee, D. Maas, and A. Vermeer, *Adv. Mater.* **22**, 3564 (2010).
- <sup>22</sup>J. R. van Ommen, D. Kooijman, M. de Niet, M. Talebi, and A. Goulas, *J. Vac. Sci. Technol. A* **33**, 021513 (2015).
- <sup>23</sup>L. F. Hakim, J. Blackson, S. M. George, and A. W. Weimer, *Chem. Vap. Deposition* **11**, 420 (2005).
- <sup>24</sup>D. M. King, J. A. Spencer, X. H. Liang, L. F. Hakim, and A. W. Weimer, *Surf. Coat. Technol.* **201**, 9163 (2007).
- <sup>25</sup>C. L. Marshall, Z. Lu, J. W. Elam, C. Nicholas, P. T. Barger, L. Abrams, A. Dameron, and R. Tracy, U.S. Patent No. 20210292258A1 (23 September 2021).
- <sup>26</sup>D. Mohanty, K. Dahlberg, D. M. King, L. A. David, A. S. Sefat, D. L. Wood, C. Daniel, S. Dhar, V. Mahajan, M. Lee, and F. Albano, *Sci. Rep.* **6**, 26532 (2016).
- <sup>27</sup>A. Yanguas-Gil, J. A. Libera, and J. W. Elam, *J. Vac. Sci. Technol. A* **39**, 062404 (2021).
- <sup>28</sup>A. Yanguas-Gil and J. W. Elam, *J. Vac. Sci. Technol. A* **32**, 031504 (2014).
- <sup>29</sup>A. Rahtu, T. Alaranta, and M. Ritala, *Langmuir* **17**, 6506 (2001).
- <sup>30</sup>NIST MS number 61313, *NIST Mass Spectrometry Data Center*, The National Institute of Standards and Technology.
- <sup>31</sup>NIST MS number 151727, *NIST Mass Spectrometry Data Center*, The National Institute of Standards and Technology.
- <sup>32</sup>T. J. Larrabee, T. E. Mallouk, and D. L. Allara, *Rev. Sci. Instrum.* **84**, 014102 (2013).
- <sup>33</sup>J.-O. Carlsson, S. Gorbalkin, D. Lubben, and J. E. Greene, *J. Vac. Sci. Technol. B* **9**, 2759 (1991).

- <sup>34</sup>J. A. McCormick, K. P. Rice, D. F. Paul, A. W. Weimer, and S. M. George, *Chem. Vapor Depos.* **13**, 491 (2007).
- <sup>35</sup>K. Manandhar, J. A. Wollmershauser, J. E. Boercker, and B. N. Feigelson, *J. Vac. Sci. Technol. A* **34**, 021519 (2016).
- <sup>36</sup>I. Iatsunskiy, M. Kempniński, M. Jancelewicz, K. Załęski, S. Jurga, and V. Smyntyna, *Vacuum* **113**, 52 (2015).
- <sup>37</sup>A. K. Shukla, A. S. Arico, K. M. E. Khatib, H. Kim, P. L. Antonucci, and V. Antonucci, *Appl. Surf. Sci.* **20**, 137 (1999).
- <sup>38</sup>H. Karhu, A. Kalantar, I. J. Väyrynen, T. Salmi, and D. Yu. Murzin, *Appl. Catal. A* **247**, 283 (2003).
- <sup>39</sup>L. Armelao, D. Belli Dell' Amico, R. Braglia, F. Calderazzo, F. Garbassi, G. Marra, and A. Merigo, *Dalton Trans.* 5559 (2009).
- <sup>40</sup>J. C. Zhou, C. M. Soto, M.-S. Chen, M. A. Bruckman, M. H. Moore, E. Barry, B. R. Ratna, P. E. Pehrsson, B. R. Spies, and T. S. Confer, *J. Nanobiotechnol.* **10**, 18 (2012).
- <sup>41</sup>M. J. Kelly, J. Kim, G. W. Roberts, and H. H. Lamb, *Top. Catal.* **49**, 178 (2008).
- <sup>42</sup>K. Ding, A. Gulec, A. M. Johnson, N. M. Schweitzer, G. D. Stucky, L. D. Marks, and P. C. Stair, *Science* **350**, 189 (2015).
- <sup>43</sup>S. Karwal, T. Li, A. Yanguas-Gil, C. P. Canlas, Y. Lei, A. U. Mane, J. A. Libera, S. Seifert, R. E. Winans, and J. W. Elam, *J. Vac. Sci. Technol. A* **36**, 01A103 (2018).
- <sup>44</sup>T. Li, S. Karwal, B. Aoun, H. Zhao, Y. Ren, C. P. Canlas, J. W. Elam, and R. E. Winans, *Chem. Mater.* **28**, 7082 (2016).
- <sup>45</sup>Z. Wu, S. Goel, M. Choi, and E. Iglesia, *J. Catal.* **311**, 458 (2014).

- <sup>46</sup>J. Cai, J. Zhang, K. Cao, M. Gong, Y. Lang, X. Liu, B. Shan, and R. Chen, *ACS Appl. Nano Mat.* **1**, 522 (2018).
- <sup>47</sup>J. Zhu, M. Yang, Y. Yu, Y. Zhu, Z. Sui, X. Zhou, A. Holmen, and D. Chen, *ACS Catal.* **5**, 6310 (2015).
- <sup>48</sup>H. Feng, J. W. Elam, J. A. Libera, W. Setthapun, and P. C. Stair, *Chem. Mater.* **22**, 3133 (2010).
- <sup>49</sup>S. Engmann, B. Ómarsson, M. Lacko, M. Stano, Š. Matejčík, and O. Ingólfsson, *J. Chem. Phys.* **138**, 234309 (2013).
- <sup>50</sup>X. H. Liang, L. B. Lyon, Y. B. Jiang, and A. W. Weimer, *J. Nanopart. Res.* **14**, 943 (2012).
- <sup>51</sup>J. W. Elam, A. Zinovev, C. Y. Han, H. H. Wang, U. Welp, J. N. Hryn, and M. J. Pellin, *Thin Solid Films* **515**, 1664 (2006).
- <sup>52</sup>D. N. Goldstein and S. M. George, *Thin Solid Films* **519**, 5339 (2011).
- <sup>53</sup>NIST MS number 37883, *NIST Mass Spectrometry Data Center*, The National Institute of Standards and Technology.
- <sup>54</sup>T. Lear, R. Marshall, J. Antonio Lopez-Sanchez, S. D. Jackson, T. M. Klapötke, M. Bäumer, G. Rupprechter, H.-J. Freund, and D. Lennon, *J. Chem. Phys.* **123**, 174706 (2005).